Far-Field Superoscillatory Metamaterial Superlens

Guanghui Yuan,[1,*] Katrine S. Rogers,[2] Edward T.F. Rogers,[3,4] and Nikolay I. Zheludev[1,3]

[1]*Centre for Disruptive Photonic Technologies, The Photonics Institute, School of Physical and Mathematical Sciences, Nanyang Technological University, 637371 Singapore*

[2]*School of Mathematics and Statistics, The Open University, Walton Hall, Milton Keynes MK7 6AA, United Kingdom*

[3]*Optoelectronics Research Centre and Centre for Photonic Metamaterials, University of Southampton, Southampton SO17 1BJ, United Kingdom*

[4]*Institute for Life Sciences, University of Southampton, Southampton SO17 1BJ, United Kingdom*

(Received 16 November 2018; revised manuscript received 12 May 2019; published 7 June 2019)

We demonstrate a metamaterial superlens: a planar array of discrete subwavelength metamolecules with individual scattering characteristics tailored to vary spatially to create subdiffraction superoscillatory focus of, in principle, arbitrary shape and size. Metamaterial free-space lenses with previously unattainable effective numerical apertures – as high as 1.52 – and foci as small as 0.33λ in size are demonstrated. Super-resolution imaging with such lenses is experimentally verified breaking the conventional diffraction limit of resolution and exhibiting resolution close to the size of the focus. Our approach will enable far-field label-free super-resolution nonalgorithmic microscopies at harmless levels of intensity, including imaging inside cells, nanostructures, and silicon chips, without impregnating them with fluorescent materials.

DOI: 10.1103/PhysRevApplied.11.064016

I. INTRODUCTION

Super-resolution optical imaging began with contact photography [1] and scanning near-field imaging (SNOM) [2], both of which register the evanescent field of the object. Although they provide unprecedented nanoscale optical resolution, near-field techniques have one very important limitation: the object has to be in nanoscale proximity to the near-field probe (in SNOM) or in direct contact with photosensitive materials (in contact photography). This excludes imaging inside cells, for instance. A number of other techniques that target recovery and recording of the evanescent field have been suggested, most notably the Veselago-Pendry "super-lens," which uses a slab of negative index metamaterial to recover evanescent waves from the object in the image plane [3]. However, implementation of these techniques faces substantial technological challenges. The triumph of the stimulated emission depletion (STED) and single-molecule localization methods (SMLM) has convincingly demonstrated that deeply subwavelength imaging is possible without capturing the evanescent fields of the object [4–6]. Indeed, these techniques only depend on the registration of the far-field light emitted by the object, while evanescent waves exponentially decay near the imaged object. However, these far-field techniques have their own limitations. STED microscopy depends on a nonlinear bleaching process requiring significant flux of light at the sample that could result in harmful modification of the object (e.g. cells), sometimes referred to as phototoxicity. Moreover, both STED and SMLM require the labeling of samples, that is, impregnating them with fluorescent dyes or quantum dots, making these techniques inapplicable for imaging solid nanostructures such as silicon chips, and limiting their biomedical use.

A type of far-field super-resolution imaging has recently been established using light diffracted from a precisely tailored mask that forms, beyond the near-field, extremely rapid local variations of electromagnetic fields, known as superoscillations. Superoscillations have local wave numbers much larger than that of a plane wave of the same frequency. This rapidly changing field can yield foci smaller than allowed by the Abbe-Rayleigh limit for a conventional lens. Superoscillatory focusing is a consequence of the superoscillation phenomenon: the mathematical paradox that within a finite interval of their argument, band-limited functions can locally oscillate much faster than the highest Fourier components in their spectra. Superoscillations were initially noticed in quantum mechanics [7]. As explained by Berry and Moiseyev, in application to optics, superoscillations are possible because in the Wigner representations the local Fourier transform of band-limited functions can have both positive and negative values, which causes subtle cancellations in the Fourier integration over all of the function [8]. The phenomenon was first experimentally observed in the diffraction of

*ghyuan@ntu.edu.sg

coherent light by a quasicrystal array of nanoholes in a metal screen and its potential for spatial and temporal super-resolution focusing and imaging without evanescent fields was recognized, see Refs. [9–14].

A mask with nanoscale-resolution optical transmission and phase retardation offers full control over a light beam, enabling superoscillatory hotspots of arbitrary shape and size [15]. Previously, however, no technology has existed that could deliver such masks with the nanoscale finesse necessary for the optical part of the spectrum. For that reason, earlier works use binary transmission and phase masks, which have substantial limitations [9,16–18]. In contrast to continuous transmission and retardation masks that offer full control of the intensities and the phases of the diffracted waves, binary masks can only control either intensity or phase in a discrete fashion, such as "yes or no" for intensity and "0 or π" for phase. An example of a binary mask is a pattern of holes in a thin opaque screen, while a patterned transparent film of appropriate thickness to induce the desired phase retardation is an example of a phase mask. Binary masks are relatively easy to manufacture with the finesse necessary to generate superoscillatory foci in the optical part of the spectrum, but their binary nature substantially limits the attainable profiles and sizes of superoscillatory hotspots, and does not allow efficient optimization of the superoscillatory trade offs between hotspot intensity, size, and field of view. However, no direct instructive mathematical algorithm exists for such optimization. Current practical implementations use various trial-and-error learning techniques that require significant computational capacity. On the other hand, explicit analytical procedures have been developed for generating arbitrary superoscillatory foci with continuous intensity and phase masks [19–25], and alternative techniques have emerged that allow semianalytical optimization of superoscillatory hotspots with preset performance characteristics such as the size, intensity, field of view, and extraneous intensity within the field of view, that are exploited below [26].

Here, we propose, fabricate, and characterize a type of metamaterial superlens that for the first time allows full control of intensities and phases of the scattered waves and, in principle, can create a hotspot of arbitrarily small size and shape. It is a planar array containing thousands of discrete subwavelength plasmonic metamolecules set in a cylindrically symmetric pattern. Each individual metamolecule has scattering characteristics tailored in such a way that the array creates a large number of interfering waves converging to a superoscillatory focus with a size that is considerable smaller than that allowed by the Abbe-Rayleigh limit. Free-space lenses with effective numerical aperture (NA, η_{NA}) as high as 1.52 (conventional limit 1), and foci as small as 0.33λ in size (conventional limit $0.5\lambda/\eta_{\mathrm{NA}}$), are reported. We also explore the gradual transformation from a conventional to a superoscillatory focus, and study lens efficiency as a function of spot size and field of view.

II. DESIGN PROCEDURES OF THE FAR-FIELD METAMATERIAL SUPERLENS

The structure of a characteristic superoscillatory focus (a hotspot) is presented in Fig. 1. The focus of a conventional lens with circular aperture of finite diameter is a familiar Airy pattern with an intense hotspot in the middle and a series of rings of increasing diameter and fading intensity. A typical superoscillatory lens (SOL) creates a more complex pattern. It contains the central hotspot with a full-width-at-half-maximum, D_N, surrounded by a zone of low intensity known as the "field of view" with characteristic diameter Δ_N, where N denotes the numbering of SOL. Here, the field of view is defined as the low-intensity zone surrounding the hotspot where light intensity does not exceed a small fraction (0.25) of the central intensity. Outside this region, a fraction of the total energy is typically diverted into broad, often high-intensity sidebands, also known as halos. The lens yield provides a measure of the fraction of energy concentrated in the central hotspot and is defined as the ratio of optical energy localized in a radius of D_N to that over the entire transverse plane. Superoscillatory lenses with small hotspots and low-intensity halos are generally preferable, but there is always a trade off between the size of the hotspot and the halo's intensity level. Depending on the application, these rich parameter fields can be even broader and may include, for instance, considerations of the chromatic performance of the lens [17].

To design the metamaterial superlens (see Fig. 1), we first construct the desired superoscillatory focus using band-limited functions, so that it can be formed by the interference of free-space waves. We then calculate the planar continuous amplitude and phase mask necessary to transform an incident plane wave into a complex wavefront, which will converge to the desired focus. Finally, we define the metasurface, a discrete array of subwavelength plasmonic metamolecules with individual scattering characteristics mimicking and matching the amplitude and phase characteristics of the continuous mask at their respective locations. We then characterize the performance of the metamaterial superlens with a coherent laser light source.

The first step in designing the metamaterial superlens is to represent the desired superoscillating field at the focus as a series of band-limited functions. Any arbitrarily two-dimensional small superoscillatory focus of radial symmetry can be constructed as a series of circular prolate spheroidal wave functions (CPSWFs) $S_i(r)$ (where i is the order), which form a complete orthogonal set both over the prescribed field of view and across the entire focal plane [26]. See the Appendix for the details.

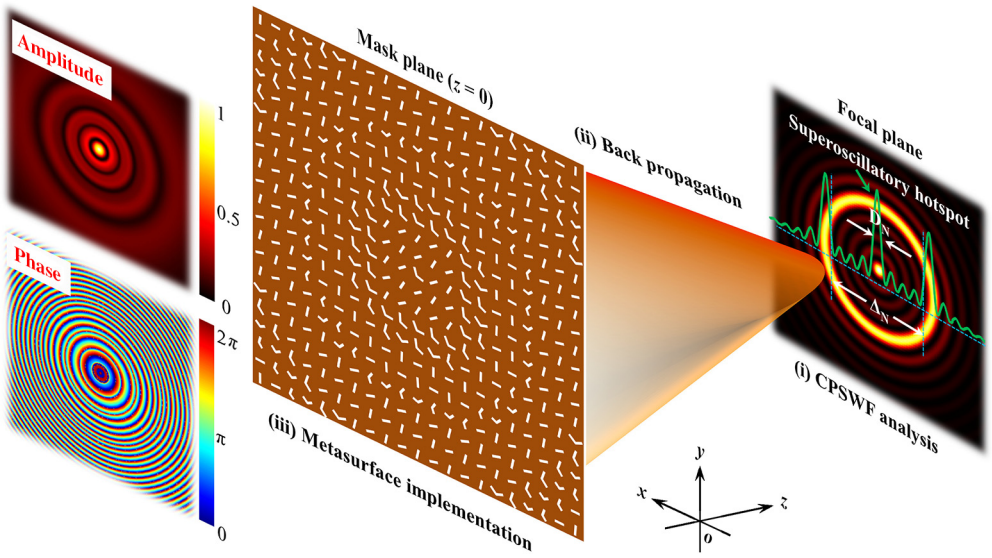

FIG. 1. Strategy for creating a far-field metamaterial superlens. (i) The electromagnetic field of the superoscillatory spots in the focal plane is chosen as a limited series of circular prolate spheroidal wave functions. (ii) The electromagnetic field distribution in the focal plane is back-propagated to the plane of the lens. This gives the required amplitude and phase profile to be imprinted on the incident wave. (iii) The lens is constructed from V shaped subwavelength metamolecules providing scattering with the required amplitude and phase to achieve the superoscillatory focus.

An important feature of this orthogonal set is that the spectrum of each $S_i(r)$ is band limited to $|k_0| = \omega/c$. However, a focus expanded as such a series of CPSWFs may only be achieved with a low yield, and a long series may be required for a good approximation. This may result in impractical yield and halo and a complex and difficult-to-construct superoscillatory mask. Instead of targeting an *a priori* prescribed hotspot, we employ a different, simplified, and more efficient strategy for producing the target hotspot. As the mask, we use a series consisting of only two (orthogonal) CPSWFs, $aS_i + S_j$, and investigate the hotpots that can be obtained by carefully balancing the relative amplitude coefficient a for different combinations of i and j. Table I summarizes the trade off between spot size, field of view, and lens yield for a range of superoscillatory foci, and also gives the relevant combinations of analytic functions representing these hotspots. See Supplemental Material for comparison of the two-CPSWF fitting results with a Gaussian function with the same size [27].

Once the superoscillatory hotspot is chosen, the entire field in the focal plane, including the hotspot, field of view, halos, and beyond, is mathematically back-propagated to the chosen location of the mask. The amplitudes and phases of the back-propagated fields at the mask plane give precise and complete information on what amplitude attenuation and phase retardation the mask should have to convert an incident plane wave into the required converging superoscillatory wavefront. To calculate the back-propagated fields, we use the angular spectrum method based on the Hankel transform, see the Appendix for the details.

III. PRECISE CONTROL OF LOCAL AMPLITUDE AND PHASE WITH PLASMONIC METASURFACE

The mask defined by this process has continuously varying transmission and retardation across the plane. Such continuous masks are very difficult to manufacture and no technology is currently available to create such masks for optical applications with the necessary finesse. Our strategy is to produce the mask using a discrete metasurface, which provides a powerful and simple way of independently controlling the transmission and retardation of the mask. We pixilate the mask into subwavelength segments and replace the continuous mask with an array of discrete scatterers (metamolecules) located in these segments with characteristics tailored to provide the same attenuation and retardation as the continuous mask. The mask is pixelated with radial symmetry, and therefore, consists of a large number of concentric rings, each containing metamolecules of the same type.

The ability to control the polarization state and phase of waves diffracted from a metamaterial array was first reported using V shape-based metamolecules in 2013 [28], and later developed into a broader concept of metasurfaces [29]. In this work, we also employ V shaped scatters. Each metamolecule is a V shaped nanoslit cut into a thin gold film, which is a simple and convenient design that can be easily adjusted to control the polarization state, intensity, and phase of the scattered wave. Individual metamolecules are characterized by the thickness of the film, t, total length of the slit, L, opening angle of the V shape, ψ, and width of the slit, d, while θ is the angle between the incident

TABLE I. Analytical formulas and yields of superoscillatory foci for different fields of view and focal spot size.

	SOL1	SOL2	SOL3	SOL4	SOL5	SOL6	SOL7
D_N (λ)	0.28	0.33	0.39	0.44	0.56	0.28	0.33
Δ_N (λ)	1.0	1.0	1.0	1.0	1.0	1.6	1.6
Mask	$1.81S_2+S_3$	$21.65S_2+S_3$	$0.57S_1+S_2$	$1.53S_1+S_2$	$7.38S_1+S_2$	$0.81S_3+S_4$	$0.18S_2+S_3$
Yield	0.06%	8.3%	35.8%	55.5%	86.1%	0.003%	1%
	SOL8	SOL9	SOL10	SOL11	SOL12	SOL13	
D_N (λ)	0.39	0.44	0.56	0.39	0.39	0.39	
Δ_N (λ)	1.6	1.6	1.6	2.0	4.0	6.0	
Mask	$2.77S_2+S_3$	$0.18S_1+S_2$	$1.48S_1+S_2$	$0.48S_2+S_3$	$0.23S_4+S_5$	$0.023S_6+S_7$	
Yield	10.2%	58%	87.1%	9.3%	2.9%	0.94%	

polarization state azimuth and the bisector of the V shape. The metasurface pattern is designed for linear incident polarization along the x direction in the chosen coordinate frame, and acts as a superoscillatory lens for y polarized transmitted light, perpendicular to the incident wave.

In an ideal superoscillatory lens, the phase and intensity of scattered light vary continuously within the prescribed range. The metamaterial mask is necessarily discretized, but approximates the continuous mask well using metamolecules with eight discrete levels of phase retardation: 0, $\pi/4$, $\pi/2$, $3\pi/4$, π, $5\pi/4$, $3\pi/2$, $7\pi/4$, and 16 levels of scattering efficiency, as shown below. To control the phase retardation of the scattered light, that is, of the light passing through the slit, we exploit the Pancharatnam-Berry phase concept [30]. Consider first straight V slits with opening angle $\psi=\pi$. For incident polarization along the x direction [E_x^i in Fig. 2(a)], the phase of x polarized transmitted light (E_x^t) is independent of slit orientation. However, we are concerned only with the performance of the metasurface lens for y polarization in which the superoscillatory focusing happens. Here, straight slits oriented at $\theta=\pi/4$ and $\theta=-\pi/4$ transmit y polarized light with a π phase difference [E_y^t and $-E_y^t$, see Fig. 2(a)]. Designs with the same orientation, θ, but progressively reduced opening angle, ψ, give differential retardation, progressively changing from that corresponding to straight slits orientation at $\theta=\pi/4$ and $\theta=-\pi/4$. Moreover, the retardation gains an additional π radians when an additional rotation of $\pi/2$ is added to the metamolecule angle, θ.

The above conceptual analysis applies to infinitely narrow slits in infinitely thin screens. In reality, the situation is more complex: the phase retardation in a V shaped slit of finite width depends on the opening angle, ψ, the length of the slit, L, and the thickness of the metal layer, which, in fact, provides a wider parameter field over which to search for the necessary retardations, and allows simplified designs of slits. Using full three-dimensional Maxwell simulations, we analyze the retardation of V shaped antennae with realistic slit widths and film thicknesses [Fig. 2(a)]. At a wavelength of 800 nm and using a gold film of thickness $t=100$ nm, eight equidistant levels of relative phase retardation, 0, $\pi/4$, $\pi/2$, $3\pi/4$, π, $5\pi/4$, $3\pi/2$, and $7\pi/4$ in the cross-polarization can be achieved with the following sets of metamolecule parameters (θ, L, ψ) respectively: ($\pi/4$, 170 nm, π), ($\pi/4$, 195 nm, π), ($\pi/4$, 220 nm, $2\pi/3$), ($\pi/4$, 300 nm, $2\pi/3$), ($-\pi/4$, 170 nm, π), ($-\pi/4$, 195 nm, π), ($-\pi/4$, 220 nm, $2\pi/3$), and ($-\pi/4$, 300 nm, $2\pi/3$).

Similarly, the intensity of the scattered light can be controlled by the length and width of the slit, the thickness of the metal layer, and the overall orientation of the metamolecules according to the $\sin(2\theta)$ dependence of the transmitted amplitude [31]. Relying mostly on this dependence, we design 16 levels of intensity variation for each retardation level, giving a palette of $2^7=8\times16$ metamolecules for use in the discretization process. The cost to pay is the loss of transmission efficiency, which is typically below 10%. We also develop a dedicated code for pixel-to-pixel pattern transfer from amplitude and phase mask parameters to the computer-aided design files used to fabricate the pixelated metalens with focused ion beam milling. During the metamaterial mask design process, we use the experimental transmission curve [27] to describe the maximum local amplitude and then to provide additional compensation by the orientation angle θ. Figure 2(b) shows an example of the SEM image and an enlarged view of one fabricated metalens for $D_8=0.39\lambda$ and $\Delta_8=1.6\lambda$ (SOL8). The resulting designs typically contain 15,366 metamolecules spread over several tens of concentric zones, each about 300-nm wide. The effect of pixilation on focusing performance is numerically studied in the Supplemental Material [27], where the pixilation mainly increases the sidelobe level and the desired superoscillatory foci can be preserved for spot size of 0.33λ and above.

IV. SUPEROSCILLATORY HOTSPOTS WITH VARYING SIZES AND FIELDS OF VIEW

Using these design principles, we have developed several superoscillatory lenses with different hotspot sizes and fields of view to illustrate the evolution from a diffraction-limited spot to a superoscillatory one (Fig. 3).

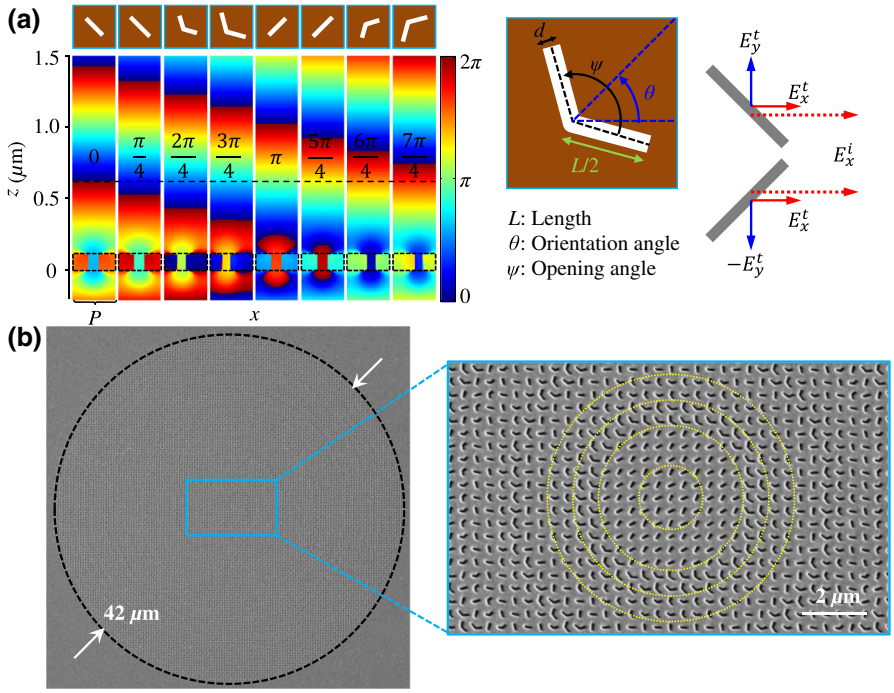

FIG. 2. (a) Details of the lens design. Eight V shaped metamolecules of different sizes, opening angles, and orientations providing different levels of phase retardation, from 0 to $7\pi/4$ (dashed reference line), are used in the lens design. Finite-difference time-domain simulations show phase distributions in the light scattered by the metamolecules located in the positions indicated by dashed boxes, and light illuminates along the z direction. Field maps for light polarized perpendicular to the incident light polarization are presented; $\lambda = 800$ nm, Period $P = 300$ nm. Top-view sketches of the metamolecule designs are shown under corresponding field maps; see details in the text. Note increased phase retardation from left to right. (b) SEM image and enlarged view of the superoscillatory metalens, fabricated by focused ion beam milling on a 100-nm-thick gold film deposited on silica glass for $D_8 = 0.39\lambda$ and $\Delta_8 = 1.6\lambda$ (SOL8). The metalens contains 15,366 metamolecules spread over 61 concentric zones (the inner four zones are highlighted with yellow dashed circles).

Note that a crosspolarizer is inserted between the lens and detector. All the lenses have an overall diameter of 42 μm and are designed to form a focus at $z = 10$ μm from the metasurface. The metamaterial superlenses are fabricated on a 100-nm-thick gold film with focused ion beam milling (see SEM images in Supplemental Material [27]). An ideal conventional lens of these dimensions would have $\eta_{\mathrm{NA}} = 0.9$, giving an Abbe-Rayleigh limited hotspot of $\lambda/(2\eta_{\mathrm{NA}}) = 0.56\lambda$.

With the superoscillatory metamaterial superlens, we achieve a factor of 2 improvement in the size of the focal spot relative to that allowed by the Abbe-Rayleigh limit. Figure 3 illustrates the performance of the full range of our metalenses (spot parameters given in Table I), with $D_N = 0.56\lambda$, 0.44λ, 0.39λ, 0.33λ, and 0.28λ for two fields of view, $\Delta_N = 1\lambda$ and 1.6λ. The effective NAs of these lenses can be evaluated by $\eta_{\mathrm{NA}}^{\mathrm{eff}} = \lambda/(2D_N)$ and range from $\eta_{\mathrm{NA}}^{\mathrm{eff}} = 0.89$ to $\eta_{\mathrm{NA}}^{\mathrm{eff}} = 1.78$. The intensity profiles in the designed transverse focal plane at $z = 10$ μm in Fig. 3(a) show a characteristic transition from conventional to superoscillatory focusing.

For the lens with $D_N = 0.56\lambda$ ($\eta_{\mathrm{NA}}^{\mathrm{eff}} = 0.89$), no significant sidebands are observed and its performance is close to that of a conventional high NA lens. The lens yield is 86.1% and 87.1% for $\Delta_5 = 1\lambda$ and $\Delta_{10} = 1.6\lambda$, respectively, compared with the encircled power ratio of 83.8% in the first dark ring of Airy disk for a conventional lens. As summarized in Table I and shown in Fig. 3, reducing D_N increases the number and intensity of concentric halos while the lens yield gradually reduces from 58% for $D_9 = 0.44\lambda$ ($\eta_{\mathrm{NA}}^{\mathrm{eff}} = 1.14$), $\Delta_9 = 1.6\lambda$ to 8.3% for $D_2 = 0.33\lambda$ ($\eta_{\mathrm{NA}}^{\mathrm{eff}} = 1.52$), $\Delta_2 = 1\lambda$. The lens yield reduces significantly for $D_N = 0.28\lambda$, reaching 0.06% and 0.003% at $\Delta_1 = 1\lambda$ and $\Delta_6 = 1.6\lambda$, respectively.

Our experimental aim is to achieve the theoretical electric field patterns and lens performance presented in Figs. 3(a) and 3(b). The experimental results are summarized in Figs. 3(c) and 3(d). The detailed experimental setup is described in the Supplemental Material [27] and Materials and Methods. Superoscillatory hotspots with $D_2 = 0.33\lambda$, $\Delta_2 = 1\lambda$ and $D_8 = 0.39\lambda$, $\Delta_8 = 1.6\lambda$ are reliably generated, although experimental reproduction of the theoretical size of the hotspot for $D_7 = 0.33\lambda$ with $\Delta_7 = 1.6\lambda$ is challenging. The asymmetry of the sidelobes along the x and y directions is caused by the depolarization effect, which happens in a high-NA focusing. Note

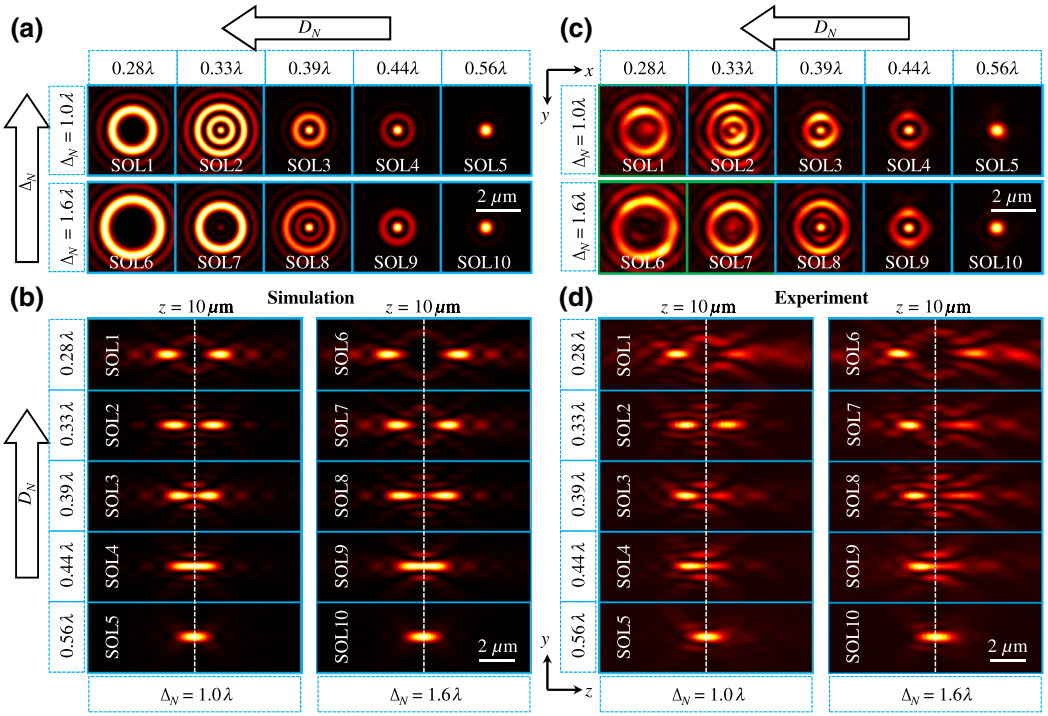

FIG. 3. Performance of superoscillatory superlenses. Simulated intensity profiles in the (a) transverse ($z = 12.5\lambda$) and longitudinal (b) planes produced by coherent light diffraction of an ideal superoscillatory mask generator. Corresponding experimentally recorded intensity profiles in the transverse (c) and longitudinal (d) planes generated by the metamaterial superlens (see Fig. 2) illuminated with a coherent laser source at $\lambda = 800$ nm.

that the hotspot of 0.33λ is smaller than the characteristic feature size of the lens design (the 300 nm $\sim 0.38\lambda$ width of the concentric rings forming the metasurface pattern). Smaller superoscillatory hotspots are significantly distorted in comparison with predicted theoretical profiles.

V. INCREASING THE FIELD OF VIEW OF SUPEROSCILLATORY HOTSPOTS

For some applications, including imaging, superoscillatory lenses with larger fields of view are more desirable, as scattering from the sidebands may distort the image. In the following, we explore to what extent an increase of the field of view affects the hotspot profile and yield of the metamaterial superlens. We demonstrate that the field of view of the metamaterial superlens can be substantially increased at the expense of lens yield, while maintaining the hotspot size. Figure 4 shows the lens performance for the fixed value of $D_N = 0.39\lambda$, while gradually increasing Δ_N = from 2λ to 6λ. As the field of view is increased and the sidebands are pushed further away, the lens yield drops from 3.7% for $\Delta_{11} = 2\lambda$, to 1.2% for $\Delta_{12} = 4\lambda$, and 0.23% for $\Delta_{13} = 6\lambda$. Note that the intensity map crosssections presented in the propagation plane are deliberately saturated to expose the structure of the superoscillatory spot in the focal plane. The experimentally recorded intensity distributions reasonably match the modeled profiles. It is important to note that the increase of the field of view reduces the lens yield, but imposes practically no degradation of the hotspot size, and in imaging applications confocal approaches can effectively suppress scattering of sidebands into the image [16], as confirmed in the imaging experiment in the next section.

VI. IMAGING WITH METAMATERIAL SUPERLENS

Due to the presence of the halo around a superoscillatory focus, simply replacing the conventional objective lens in a wide-field microscope with a superoscillatory lens is only practical for objects that are smaller than the field of view. This is because the halo will be present in the image, distorting it. For universal imaging applications, the effect of the halo can, however, be mitigated by using a superoscillatory lens for structured illumination combined with confocal detection. In this configuration, a conventional lens with high NA is used as the objective lens, while the object is illuminated by a superoscillatory lens with subdiffraction focus. A small confocal aperture is used to detect only the central part of the image, thus excluding the halo. Imaging is achieved by two-dimensional raster scanning of the sample on a piezo-stage. To demonstrate the imaging performance of the metamaterial superlenses, we use such a confocal arrangement

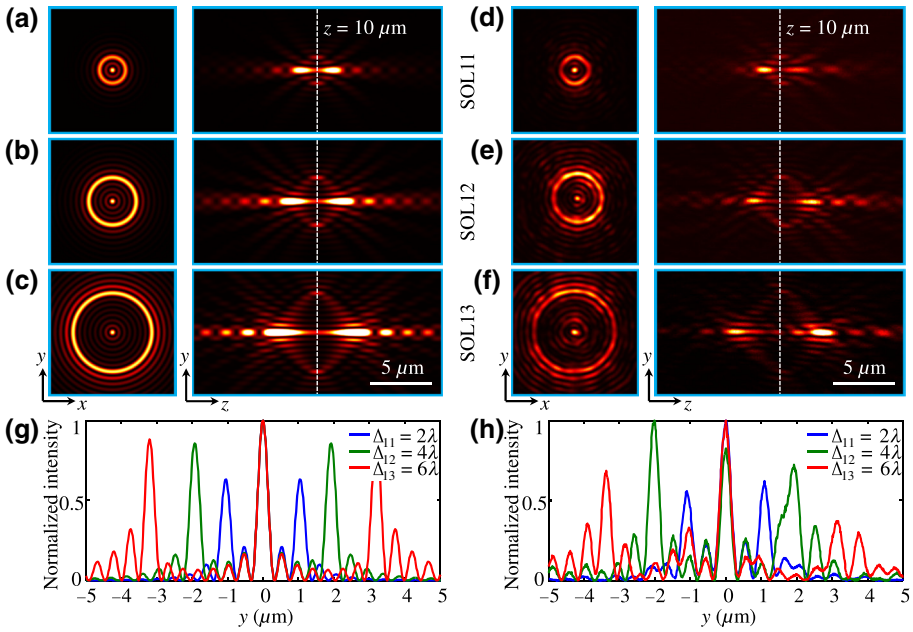

FIG. 4. Performance of superoscillatory superlenses with larger field of view. Simulated superoscillatory spot crosssections for $D_N = 0.39\lambda$ and varying $\Delta_N = 2\lambda$ (a), 4λ (b) and 6λ (c) in the transverse and longitudinal planes of the lens. Corresponding experimentally recorded intensity profiles (d–f) in the transverse and longitudinal planes generated by the metamaterial superlens illuminated with a coherent laser source at $\lambda = 800$ nm. (g),(h) Normalized line-scan intensity profiles at the focal plane $z = 10$ μm (indicated by vertical dashed lines): simulation (g) and experiment (h).

with a 100× objective lens ($\eta_{NA} = 0.9$) and an avalanche photodiode.

The limits of resolution of metamaterial lenses are tested on pairs of nanoholes with variable distance between the holes and starlike arrangements of nanoholes perforated by focused ion beam milling in opaque screen (100-nm-thick gold film on glass substrate). Figure 5(a) illustrates that for a given field of view of the superlens, the decrease of superoscillatory illumination hotspot size results in an increase of resolution: while a pair of holes with center-to-center separation of 0.4λ is not resolved by a metamaterial superlens with the hotspot diameter of 0.56λ, it is increasingly better resolved with metamaterial superlenses with hotspots of 0.39λ and 0.33λ.

Here, we shall note that a pair of holes with center-to-center separation of 0.4λ is not resolved by confocal imaging with the same objective lens ($\eta_{NA} = 0.9$) with flat bright-field illumination as illustrated by the last column in Fig. 5. Figure 5(b) illustrates high-quality imaging of an extended object of overall size of approximately 3λ, that is, much higher than the field of view of the lens, confirming that the halo of the illumination profile is efficiently suppressed in the confocal regime.

We test the resolution of the metamaterial superlenses with a larger field of view (SOL11-13) by resolving a set of hole pairs with different separations. Figure 5(c) illustrates that resolution of the metamaterial superlens does not depend on the field of view and is mainly controlled by the hotspot size. Indeed, images of hole pairs with variable center-to-center distance are resolved at the level when the hotspot diameter becomes smaller than the distance between the holes (0.4λ), regardless the field of view of the lens. However, a larger field of view results in a weaker hotspot and deterioration of the signal-to-noise ratio, as evident by comparison of the images in Fig. 5(c). It is worth noting that the resolved gap size is 120 nm ($\lambda/6.7$), which is better than the $\lambda/6$ reported in our previous work [16].

From here, we can conclude that resolution of imaging with superoscillatory illumination using metamaterial superlens is approximately the size of the superoscillatory hotspot of the lens and beats the "diffraction limit" attainable with bright-field illumination. This can be additionally illustrated by analyzing the profile of the image of an individual hole [see Fig. 5(a), image with $D_N = 0.33\lambda$]. Indeed, a convolution of the hole size of 160 nm and the hotspot size of 264 nm (0.33λ) will return an image of 284 nm in diameter, that is close to the observed 272-nm FWHM diameter of the experimentally recorded image [Fig. 5(a)].

VII. DISCUSSION

Our work provides a proof-of-principle demonstration that a far-field metamaterial superlens can arbitrarily control the intensity and phase of scattered light and can, therefore, mimic complex continuous superoscillatory masks. We have shown that such superlenses can be engineered and manufactured with precision sufficient to generate superoscillatory hotspots as small as 0.33λ with a corresponding effective NA of $\eta_{NA}^{eff} = 1.52$ and a level of yield acceptable for imaging applications. This is far beyond what it is possible to achieve in free space with conventional lenses. Indeed, conventional lenses are limited to $\eta_{NA} = 1$ in free space and approaching this limit requires expensive, complex, and bulky lenses. Compared with the superoscillatory lenses and Toraldo-type binary filters that control either phase or intensity of light, the metamaterial

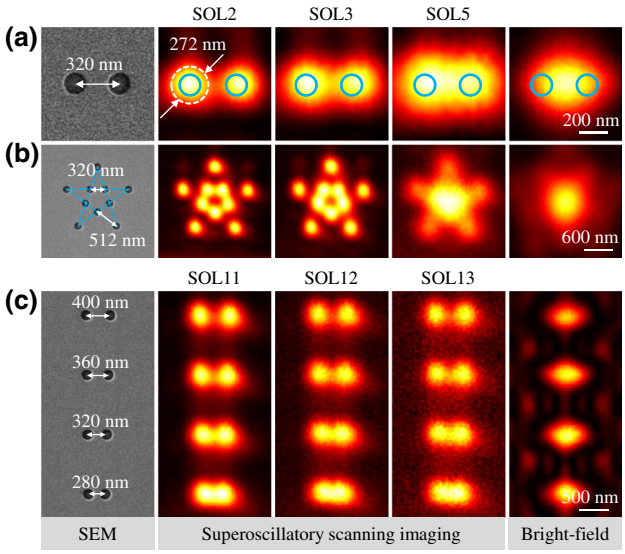

FIG. 5. Imaging with metamaterial superlenses at the wavelength of $\lambda = 800$ nm. The first column shows SEM images of the test samples: (a) a pair of holes with diameters of 160 nm and center-to-center separations of 320 nm (0.4λ), (b) a star-shaped constellation of holes, each with a 160-nm diameter. (c) Pairs of holes with diameters of 160 nm with separations of 400 nm (0.5λ), 360 nm (0.45λ), 320 nm (0.4λ), and 280 nm (0.35λ). Rows (a-b) shows imaging results with superoscillatory illumination using metamaterial superlenses with different hotspot sizes of $D_N = 0.33\lambda$ (SOL2), 0.39λ (SOL3), 0.56λ (SOL5), and identical field of view $\Delta_N = 1\lambda$. Row (c) shows imaging results with superoscillatory illumination using metamaterial superlenses with different fields of view $\Delta_N = 2\lambda$ (SOL11), 4λ (SOL12), 6λ (SOL13), and identical hotspot size of $D_N = 0.39\lambda$.

superlens can control intensity and phase independently. This offers better performance and ultimate flexibility for designing compact focusing solutions for subwavelength hotspots for imaging applications. Although the efficiency of the metamaterial superlenses using plasmonic V shaped antennas is limited, it can be improved by using high-throughput dielectric metasurfaces. We prove the practicality of imaging using a number of metamaterial lenses with different fields of view and effective NAs, demonstrating resolution close to the size of superoscillatory hotspot and beating the conventional "diffraction limit." Imaging of more complex objects like living cells or silicon photonic chips with superoscillatory lenses is practical [32,33]. Importantly, ultrathin superoscillatory metamaterial superlenses, which are capable of continuous amplitude and phase modulation, can be manufactured by well-established high-throughput nanomanufacturing processes such as high-resolution lithography and can be easily scalable to operate at any wavelength. Creating superoscillatory fields with metasurfaces appears to be a very powerful concept that goes beyond generating subdiffraction hotspots and imaging. Indeed, a recent paper has demonstrated the use of phase singularities in optical field generated by a Pancharatnam-Berry metasurface in optical nanometrology [34]. The data from this paper can be obtained from the University of Southampton ePrints research repository [35].

ACKNOWLEDGMENTS

This work was supported by the Singapore Ministry of Education (Grant No. MOE2016-T3-1-006), the Agency for Science, Technology and Research (A*STAR) Singapore (Grant No. SERC A1685b0005), the Engineering and Physical Sciences Research Council UK (Grants No. EP/N00762X/1 and No. EP/M0091221) and Wessex Medical Research (Grant No. WM03).

APPENDIX

1. Optimization of superoscillatory spots

Following Ref. [26], our two-dimensional superoscillatory fields $E(r)$ with radial symmetry, predefined spot size (D_N), and field of view (Δ_N) are constructed from a linear combination of two band-limited circular prolate spheroidal wave functions, $S_n(r)$ and $S_m(r)$

$$E(r) = aS_n(r) + S_m(r), \tag{A1}$$

where a is the relative coefficient, which is optimized to minimize the difference between the FWHM of the superoscillatory intensity profile $I(r) = |E(r)|^2$ and the desired D_N. $S_n(r)$ and $S_m(r)$ satisfy the following eigenvalue problem and can be calculated following Ref. [36]

$$\int_0^1 uJ_q(cur)S_i(r)du = \beta_{i,c}^q S_i(r), \tag{A2}$$

where $J_q(\cdot)$ is the Bessel function of the first type and order q (here, $q = 0$ throughout, as this returns functions bandlimited under the Hankel Transform), $c = k_0\Delta_N$ is the bandwidth parameter and $k_0 = 2\pi/\lambda$ is the free-space wavevector. Reference [26] describes the algorithm for selecting the function orders n and m.

2. Generation of superoscillatory masks

Given that the complex superoscillatory field $E(r)$ over the whole focal plane is obtained from Eq. (A1), we can back-propagate the field to obtain the required superoscillatory mask using the angular spectrum method. The angular spectrum at the focal plane ($z = z_f$) is given by the following Fourier transform

$$A(f_x, f_y)|_{z=z_f} = \int\int_{-\infty}^{\infty} E(x, y, z_f) \times \exp[-i2\pi(f_x x + f_y y)]dxdy. \tag{A3}$$

In polar coordinates, $x = r\cos\theta, y = y\sin\theta$, $dxdy = rdrd\theta$, $f_x = f_r\cos\varphi, f_y = f_r\sin\varphi$. After this coordinate transformation, Eq. (A3) can be simplified to

$$\begin{aligned} A(f_x,f_y)|_{z=z_f} &= \int_0^{\infty} E(r)\left\{\int_0^{2\pi}\exp[-i2\pi rf_r \right. \\ &\quad \left.\times\cos(\theta-\varphi)]d\theta\right\}rdr, \\ &= 2\pi\int_0^{\infty} E(r)J_0(2\pi rf_r)rdr \\ &= 2\pi * \mathrm{HT}_0[E(r)] = A(f_r), \end{aligned} \tag{A4}$$

where $\mathrm{HT}_0[\cdot]$ is the zero-order Hankel transform and the integral kernel $J_0(\cdot)$ is the Bessel function of zero order. Therefore, the angular spectrum at the mask plane ($z = 0$) is given by

$$A(f_x,f_y)|_{z=0} = A(f_r)\exp\left(-2\pi i\sqrt{1/\lambda^2 - f_r^2}z_f\right), \tag{A5}$$

where the second term represents the back-propagation phase factor. Hence, the electric field distribution at the mask plane can be expressed as

$$\begin{aligned} &E_0(x,y,0) \\ &= \int\int A(f_x,f_y)|_{z=0}\cdot\exp[i2\pi(f_x x + f_y y)]df_x df_y, \\ &= \int_0^{f_{\max}} A(f_r)\exp\left(-2\pi i\sqrt{1/\lambda^2 - f_r^2}z_f\right) \\ &\quad\times\left\{\int_0^{2\pi}\exp[i2\pi rf_r\cos(\theta-\alpha)]d\alpha\right\}f_r df_r, \\ &= 2\pi\int_0^{f_{\max}} A(f_r)\exp\left(-2\pi i\sqrt{1/\lambda^2 - f_r^2}z_f\right) \\ &\quad\times J_0(2\pi rf_r)f_r df_r, \\ &= 2\pi * \mathrm{IHT}_0\left[A(f_r)\exp\left(-2\pi i\sqrt{1/\lambda^2 - f_r^2}z_f\right)\right], \end{aligned} \tag{A6}$$

where $\mathrm{IHT}_0[\cdot]$ is the zero-order inverse Hankel transform, $f_{\max} = \eta_{\mathrm{NA}}/\lambda$ is the maximum spatial frequency, and η_{NA} is the numerical aperture. Note that the spectrum is band-limited to $[-f_{\max}, f_{\max}]$.

[1] S. Y. Chou, P. R. Krauss, and P. J. Renstrom, Imprint of sub-25 nm vias and trenches in polymers, Appl. Phys. Lett. **67**, 3114 (1995).

[2] D. W. Pohl, W. Denk, and M. Lanz, Optical stethoscopy: Image recording with resolution λ/20, Appl. Phys. Lett. **44**, 651 (1984).

[3] J. B. Pendry, Negative Refraction Makes a Perfect Lens, Phys. Rev. Lett. **85**, 3966 (2000).

[4] S. W. Hell, Far-field optical nanoscopy, Science **316**, 1153 (2007).

[5] E. Betzig, G. H. Patterson, R. Sougrat, O. W. Lindwasser, S. Olenych, J. S. Bonifacino, M. W. Davidson, J. Lippincott-Schwartz, and H. F. Hess, Imaging intracellular fluorescent proteins at nanometer resolution, Science **313**, 1642 (2006).

[6] M. J. Rust, M. Bates, and X. Zhuang, Sub-diffraction-limit imaging by stochastic optical reconstruction microscopy (STORM), Nat. Methods **3**, 793 (2006).

[7] Y. Aharonov, D. Z. Albert, and L. Vaidman, How the Result of a Measurement of a Component of the Spin of a Spin-1/2 Particle can Turn Out to be 100, Phys. Rev. Lett. **60**, 1351 (1988).

[8] M. V. Berry and N. Moiseyev, Superoscillations and supershifts in phase space: Wigner and Husimi function interpretations, J. Phys. A: Math. Theor. **47**, 315203 (2014).

[9] E. T. F. Rogers and N. I. Zheludev, Optical super-oscillations: Sub-wavelength light focusing and super-resolution imaging, J. Opt. **15**, 094008 (2013).

[10] G. Gbur, Using superoscillations for superresolved imaging and subwavelength focusing, Nanophotonics **8**, 205 (2019).

[11] A. M. H. Wong and G. V. Eleftheriades, Superoscillations without sidebands: Power-efficient sub-diffraction imaging with propagating waves, Sci. Rep. **5**, 8449 (2015).

[12] Y. Kozawa, D. Matsunaga, and S. Sato, Superresolution imaging via superoscillation focusing of a radially polarized beam, Optica **5**, 86 (2018).

[13] T. Zacharias, B. Hadad, A. Bahabad, and Y. Eliezer, Axial sub-Fourier focusing of an optical beam, Opt. Lett. **42**, 3205 (2017).

[14] Y. Eliezer, L. Hareli, L. Lobachinsky, S. Froim, and A. Bahabad, Breaking the Temporal Resolution Limit by Superoscillating Optical Beats, Phys. Rev. Lett. **119**, 043903 (2017).

[15] F. M. Huang and N. I. Zheludev, Super-resolution without evanescent waves, Nano Lett. **9**, 1249 (2009).

[16] E. T. F. Rogers, J. Lindberg, T. Roy, S. Savo, J. E. Chad, M. R. Dennis, and N. I. Zheludev, A super-oscillatory lens optical microscope for subwavelength imaging, Nat. Mater. **11**, 432 (2012).

[17] G. H. Yuan, E. T. F. Rogers, and N. I. Zheludev, Achromatic super-oscillatory lenses with sub-wavelength focusing, Light Sci. Appl. **6**, e17036 (2017).

[18] G. Chen, Y. Li, X. Wang, Z. Wen, F. Lin, L. Dai, L. Chen, Y. He, and S. Liu, Super-oscillation far-field focusing lens based on ultra-thin width-varied metallic slit array, IEEE Photonics Technol. Lett. **28**, 335 (2016).

[19] W. Qiao, A simple model of Aharonov–Berry's superoscillations, J. Phys. A: Math. Gen. **29**, 2257 (1996).

[20] P. J. S. G. Ferreira, A. Kempf, and M. J. C. S. Reis, Construction of Aharonov–Berry's superoscillations, J. Phys. A: Math. Theor. **40**, 5141 (2007).

[21] D. G. Lee and P. J. S. G. Ferreira, Direct construction of superoscillations, IEEE Trans. Signal Process. **62**, 3125 (2014).

[22] K. Huang, H. Liu, F. J. Garcia-Vidal, M. H. Hong, B. Luk'yanchuk, J. H. Teng, and C.-W. Qiu, Ultrahigh-capacity

non-periodic photon sieves operating in visible light, Nat. Commun. **6**, 7059 (2015).

[23] D. M. de Juana, J. E. Oti, V. F. Canales, and M. P. Cagigal, Design of superresolving continuous phase filters, Opt. Lett. **28**, 607 (2003).

[24] K. G. Makris and D. Psaltis, Superoscillatory diffraction-free beams, Opt. Lett. **36**, 4335 (2011).

[25] E. Greenfield, R. Schley, I. Hurwitz, J. Nemirovsky, K. G. Makris, and M. Segev, Experimental generation of arbitrarily shaped diffractionless superoscillatory optical beams, Opt. Express **21**, 13425 (2013).

[26] K. S. Rogers, K. N. Bourdakos, G. H. Yuan, S. Mahajan, and E. T. F. Rogers, Optimising superoscillatory spots for far-field super-resolution imaging, Opt. Express **26**, 8095 (2018).

[27] See Supplemental Material at http://link.aps.org/supplemental/10.1103/PhysRevApplied.11.064016 for details on the optimization of super-oscillatory hotspots, mask generation, amplitude control of the metamolecule, pixelation effect, sample SEM images and experimental setup.

[28] A. Papakostas, A. Potts, D. M. Bagnall, S. L. Prosvirnin, H. J. Coles, and N. I. Zheludev, Optical Manifestations of Planar Chirality, Phys. Rev. Lett. **90**, 107404 (2003).

[29] N. F. Yu, P. Genevet, M. A. Kats, F. Aieta, J. P. Tetienne, F. Capasso, and Z. Gaburro, Light propagation with phase discontinuities: generalized laws of reflection and refraction, Science **334**, 333 (2011).

[30] Z. Bomzon, G. Biener, V. Kleiner, and E. Hasman, Space-variant Pancharatnam-Berry phase optical elements with computer-generated subwavelength gratings, Opt. Lett. **27**, 1141 (2002).

[31] L. X. Liu, X. Q. Zhang, M. Kenney, X. Q. Su, N. N. Xu, C. M. Ouyang, Y. L. Shi, J. G. Han, W. L. Zhang, and S. Zhang, Broadband metasurfaces with simultaneous control of phase and amplitude, Adv. Mater. **26**, 5031 (2014).

[32] E. T. F. Rogers, S. Quraishe, J. E. Chad, T. A. Newman, N. I. Zheludev, and P. J. S. Smith, New super-oscillatory technology for unlabelled super-resolution cellular imaging with polarisation contrast, Biophys. J. **112**, 186A (2017).

[33] M. Berry *et al.*, Roadmap on superoscillations, J. Opt. **21**, 053002 (2018).

[34] G. H. Yuan and N. I. Zheludev, Detecting nanometric displacements with optical ruler metrology, Science **364**, 771 (2019).

[35] Guanghui Yuan, Katrine S. Rogers, Edward T. F. Rogers, and Nikolay I. Zheludev, Data for: "Far-field superoscillatory metamaterial superlens," http://dx.doi.org/10.5258/SOTON/D0462 (2019).

[36] A. Karoui and T. Moumni, Spectral analysis of the finite Hankel transform and circular prolate spheroidal wave functions, J. Comput. Appl. Math. **233**, 315 (2009).